

# Cold flow analysis of trapped vortex combustor using two equation turbulence models

P. Selvaganesh and S. Vengadesan

Department of Applied Mechanics  
Indian Institute of Technology Madras  
Chennai, India

## ABSTRACT

A new combustor concept referred as the trapped vortex combustor (TVC) employs a vortex that is trapped inside a cavity to stabilise the flame. The cavity is formed between two axisymmetric disks mounted in tandem. TVC offers many advantages when compared to conventional swirl stabilisers. In the present work, numerical investigation of cold flow (non-reacting) through trapped vortex combustor is performed. The numerical simulation involves passive flow through TVC to obtain an optimum cavity size to trap stable vortices inside the cavity and to observe the important characteristics of TVC. One of the main objectives is to evaluate various two equation turbulence models for the aerodynamic predictions of TVC. Commercial CFD software Fluent is used for the present study. In addition to many models available, Non-linear  $k-\omega$  and modified  $k-\omega$  models are incorporated through user defined functions. Results obtained include streamlines, residence time and entrainments for all models. The reattachment length obtained by non-linear  $k-\omega$  model closely matches with that obtained by DNS in the case of forebody-spindle alone. Non-linear  $k-\omega$  model alone captures the corner vortices while all the other models failed to capture. From the entrainment characteristics study, it is inferred that the primary air needs to be injected for accommodating the decrease in oxidizer inside the cavity to obtain better performance from the TVC.

## NOMENCLATURE

$C_D$	coefficient of drag
$\Delta C_D$	change in drag coefficient
$C_f$	skin friction coefficient
$C_p$	pressure coefficient
$D_0$	diameter of flat cylindrical forebody
$D_d$	diameter of cylindrical afterbody
$D_s$	diameter of spindle
$h$	step height of backward facing step
$k$	turbulent kinetic energy
$P$	average pressure
$r$	radial direction
Re	Reynolds number
$t_c$	calculated time
$\overline{u_i' u_j'}$	Reynolds stress
$U$	freestream velocity
$U_i$	average velocity
$y^+$	dimensionless distance to wall
$z$	axial direction
$Z_c$	size of the cavity

## Greek symbols

$\nu$	kinematic viscosity
$\rho$	density
$\omega$	turbulent specific dissipation rate
$\varepsilon$	turbulent dissipation rate

## Abbreviations

BFS	backward facing step
CFDC	computational fluid dynamics with chemistry
DNS	direct-numerical simulation
LES	large eddy simulation
LEM	linear eddy model
LRN	low Reynolds number
QUICK	quadratic upwind interpolation for convective kinematics
RANS	Reynolds-averaged Navier-Stokes equations
SIMPLE	semi-implicit method for pressure linked equations
TVC	trapped vortex combustor
UDF	user defined functions
URANS	unsteady Reynolds-averaged Navier-Stokes equations

## 1.0 INTRODUCTION

Today, military aircraft must fly farther, faster, and with ever-increasing payloads and mission capability. But the unsteady flow in aircraft combustors limits fuel-lean operation and influences the flame-stability characteristics. Flame instabilities in the combustor can lead to significant performance degradation, possible blow out, structural vibration and even catastrophic failure. Combustion stability can be achieved using recirculation zones so as to provide continuous source of ignition by mixing hot products and burning gases with the incoming fuel and air. Swirl vanes, bluff bodies, and rearward facing steps are commonly used methods of establishing recirculation zones for flame stabilisation. Recently, a simple, compact, and an efficient method of using cavity to stabilise combustion was proposed by Hsu *et al.*<sup>(2)</sup>. This new combustor concept employs a vortex that is trapped inside a cavity to stabilise the flame, and hence, is referred as the trapped vortex combustor (TVC).

To fully predict the combustion characteristics of TVC and the interaction between the chemical species, the fluid mechanics associated must be accurately simulated. There are several methods available for modeling or simulating these processes: Direct numerical simulation (DNS), Large eddy simulation (LES), Reynolds averaged Navier-Stokes (RANS) models.

DNS resolves the flow to sufficiently fine detail to capture the motion of the smallest eddies and the briefest time-scales. For most practical combustion systems with high Reynolds number, this is extremely computationally expensive. LES uses the supposition that most of the flow energy is contained in the largest eddies, and only flow features on the scale of the largest eddies are calculated. A model is used to account for the stresses generated in the flow by eddies which are smaller than this scale. RANS calculate mean flow parameters. In the averaging process used to generate mean flow equations, information regarding turbulent fluctuations is lost. This loss of information is manifested by the second moments of fluctuating velocity or 'Reynolds stresses' which appear explicitly in the mean flow equations. The task of a turbulence model is to find an adequate numerical representation of these Reynolds stresses. DNS and LES are valuable for providing flow details which are difficult or impossible to measure experimentally. But engineers would usually prefer to work with mean quantities rather than instantaneous quantities. This provides the motivation for the present work.

A brief review of the available literature on the experimental work and the numerical simulation of trapped vortex-combustor is given below.

Little and Whipkey's<sup>(6)</sup> research concerned with the drag and the flow characteristics of locked vortex afterbody shapes formed by thin disks spaced along a central spindle. Their interest was to develop drag reduction concepts for conventional aircraft afterbodies. They showed that the minimum drag corresponds to the condition where the recirculation zone is stable.

Hsu *et al.*<sup>(2)</sup> studied the combustion characteristics of trapped vortex combustor. They observed the effect of cavity length on the pressure drop across the combustor. As the cavity length is varied, the pressure drop is observed to pass through a minimum at a cavity length of 0.6 times the diameter of forebody for the non-reacting case. Primary air and gaseous propane are injected directly into the cavity through a multiple jets located on the upstream of the afterbody in order to improve the performance. Very low overall lean blow out equivalence ratios are obtained for the TVC over a wide range of annular and primary airflow rates.

Katta and Roquemore<sup>(3)</sup> used a third order accurate time dependent computational fluid dynamics with chemistry (CFDC) code to predict the results of Little and Whipkey<sup>(6)</sup> and of Hsu *et al.*<sup>(2)</sup>. They tried with standard isotropic  $k$ - $\varepsilon$  model with wall function approach to predict the characteristics of TVC for the cold flow case. They arrived a optimum cavity size that corresponds to the minimum drag when the vortex is stable inside the cavity. They also reported that the turbulence model seems to dissipate the corner vortices that are observed in the direct simulations. They found that a stationary vortex yields minimum mass exchange between the vortex and the main flow.

Katta and Roquemore<sup>(4)</sup> investigated the vortex dynamics of a cavity into which fluid mass is directly injected through jets. CFDC was used for simulating the dynamic flows associated with an axisymmetric, centerbody trapped vortex combustor under non-reacting and reacting conditions. They also found that mass addition has a stabilizing effect on the flow in the optimum cavity size and a destabilizing effect in other than optimum cavity size.

Stone and Menon<sup>(9)</sup> simulated fuel/air mixing and combustion in a TVC using large eddy simulation (LES). They investigated the effect of Reynolds number on fuel/air mixing and combustion properties. They developed a new subgrid mixing model for LES using linear eddy model (LEM) to study the turbulent mixing properties of TVC under non-reacting conditions.

From the above literature, it is observed that, the characteristics of TVC were studied by experiment, DNS and LES. But DNS and LES are computationally expensive. In this paper, important properties of TVC are studied using two equation turbulence models. Their predictive capability and applicability is evaluated.

### 1.1 Objective

The objective of the present work is to study the characteristics of trapped vortex combustor under cold flow (non-reacting) condition using  $k$ - $\omega$  family of turbulence models. Since from literature, it is observed that  $k$ - $\omega$  gives better results than  $k$ - $\varepsilon$  for the adverse pressure gradient and separated flows. They are also reported to have better numerical stability. For this, modified  $k$ - $\omega$ , of Bredberg *et al.*<sup>(1)</sup> which has a cross diffusion term in the  $\omega$  equation and the non-linear  $k$ - $\omega$  of Song and Amano<sup>(8)</sup> which has non-linear terms in the eddy viscosity hypothesis are used to solve the unsteady Reynolds averaged Navier-Stokes (URANS) equations.

The above models have not been previously tested for combustion flow. The non-linear  $k$ - $\omega$  and the modified  $k$ - $\omega$  models are incorporated in commercial solver FLUENT using user defined functions (UDFs). The geometry considered in this work is the same as the one considered by Katta and Roquemore<sup>(3)</sup>. Results obtained by  $k$ - $\omega$  models are compared with those by DNS reported by Katta and Roquemore<sup>(3)</sup>. This allows a critical evaluation to be made about the capability of turbulence models to predict such flows accurately.

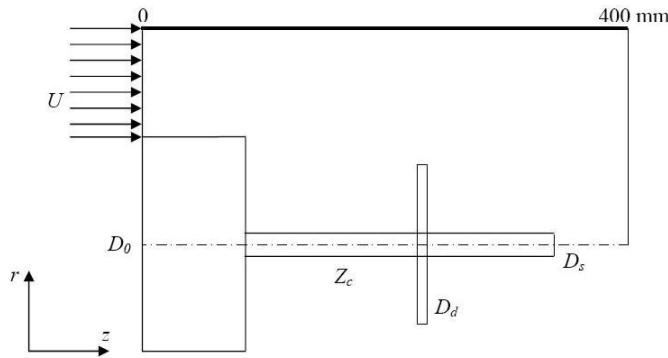


Figure 1. Schematic representation of trapped vortex combustor.

## 2.0 FORMULATION AND SOLUTION METHODOLOGY

The geometry chosen for the study of aerodynamic effects on a bluff forebody is very similar to that used by Katta and Roquemore<sup>(3)</sup>. The geometry shown in Fig. 1 consists of a 100mm diameter flat cylindrical forebody ( $D_0$ ) enclosed in an annular cylindrical tube having a 200mm inner diameter. An afterbody disk having a diameter ( $D_d$ ) of 75mm and a thickness of 2mm is attached to the forebody using spindle. The spindle has a diameter ( $D_s$ ) of 28mm. A cavity of size ( $Z_c$ ) is formed between the forebody and the afterbody disk.

### 2.1 Governing equations

For unsteady incompressible turbulent flows, the averaged governing equations in an arbitrary coordinate system are written as follows:

$$\frac{\partial U_i}{\partial x_i} = 0 \quad \dots (1)$$

$$\frac{\partial U_i}{\partial t} + \frac{\partial U_j U_i}{\partial x_j} = -\frac{1}{\rho} \frac{\partial P}{\partial x_i} + \frac{\partial}{\partial x_j} \left( \nu \frac{\partial U_i}{\partial x_j} - \overline{u'_i u'_j} \right) \quad \dots (2)$$

where,  $x_i$  is the spatial co-ordinate,  $t$  is the time,  $U_i$  is the averaged velocity,  $P$  is the averaged pressure,  $\rho$  is the fluid density,  $\nu$  is molecular kinematic viscosity. Because of the averaging process, the loss of information regarding the turbulent fluctuations is appeared in the form of Reynolds stress which is given by  $-\overline{u'_i u'_j}$ .

The resulting Reynolds stresses are modeled and the transport equations for standard two equation models are available in standard text books<sup>(7 & 10)</sup> and governing equations for modified  $k$ - $\omega$  and non-linear low-Re  $k$ - $\omega$  model are given in the following.

#### 2.1.1 Modified $k$ - $\omega$ model

The transport equation for  $k$  and  $\omega$

$$\frac{D\rho k}{Dt} = P_k - C_k \rho k \omega + \frac{\partial}{\partial x_j} \left[ \left( \mu + \frac{\mu_t}{\sigma_k} \right) \frac{\partial k}{\partial x_j} \right] \quad \dots (3)$$

$$\frac{D\rho \omega}{Dt} = C_{\omega 1} \rho \frac{\omega}{k} P_k - C_{\omega 2} \rho \omega^2 + C_{\omega 3} \left( \frac{\mu}{k} + \frac{\mu_t}{k} \right) \frac{\partial k}{\partial x_j} \frac{\partial \omega}{\partial x_j} \quad \dots (4)$$

$$+ \frac{\partial}{\partial x_j} \left[ \left( \mu + \frac{\mu_t}{\sigma_\omega} \right) \frac{\partial \omega}{\partial x_j} \right]$$

The eddy viscosity is given by

$$\mu_t = C_\mu f_\mu \rho \frac{k}{\omega} \quad \dots (5)$$

The damping function is given by

$$f_\mu = 0.09 + \left( 0.91 + \frac{1}{\text{Re}_t^3} \right) \left[ 1 - \exp \left\{ - \left( \frac{\text{Re}_t}{25} \right)^{2.75} \right\} \right] \quad \dots (6)$$

Turbulent Reynolds number is given by  $\text{Re}_t = \frac{k}{\omega \nu}$   
And the closure coefficients are

$$C_k = 0.09, C_\mu = 1, C_\omega = 1.1, C_{\omega 1} = 0.49, C_{\omega 2} = 0.072, \sigma_k = 1.1, \sigma_\omega = 1.8$$

#### 2.2.2 Non-linear $k$ - $\omega$ model

The equations for kinetic energy and specific dissipation rate are given as

$$\frac{D\rho k}{Dt} = P_k + \frac{\partial}{\partial x_j} \left[ \left( \mu + \frac{\mu_t}{\sigma_k} \right) \frac{\partial k}{\partial x_j} \right] - \rho \beta^* k \omega \quad \dots (7)$$

$$\frac{D\rho \omega}{Dt} = \alpha \frac{\omega}{k} P_k + \frac{\partial}{\partial x_j} \left[ \left( \mu + \frac{\mu_t}{\sigma_\omega} \right) \frac{\partial \omega}{\partial x_j} \right] - \rho \beta \omega^2 \quad \dots (8)$$

Reynolds stress is given by

$$-\rho \overline{u'_i u'_j} = -\frac{2}{3} \rho \delta_{ij} k + \mu_t \left( \frac{\partial U_i}{\partial x_j} + \frac{\partial U_j}{\partial x_i} \right) \quad \dots (9)$$

$$+ C_1 \frac{\mu_t}{\omega} \left( S_{ik} S_{kj} - \frac{1}{3} S_{kl} S_{kl} \delta_{ij} \right)$$

$$+ C_2 \frac{\mu_t}{\omega} \left( \Omega_{ik} S_{kj} + \Omega_{jk} S_{ki} \right) + C_3 \frac{\mu_t}{\omega} \left( \Omega_{ik} \Omega_{kj} - \frac{1}{3} \Omega_{kl} \Omega_{kl} \delta_{ij} \right)$$

the production term is given by

$$P_k = -\rho \overline{u'_i u'_j} \frac{\partial U_i}{\partial x_j} \quad \dots (10)$$

and other parameters are given by

$$\alpha^* = \frac{\alpha_0^* + \text{Re}_t / R_k}{1 + \text{Re}_t / R_k};$$

$$\alpha = \frac{5}{9} \frac{\alpha_0^* + \text{Re}_t / R_\omega}{1 + \text{Re}_t / R_\omega} (\alpha^*)^{-1};$$

$$\beta^* = \frac{9}{100} \frac{5/18 + (\text{Re}_t / R_\beta)^4}{1 + (\text{Re}_t / R_\beta)^4}$$

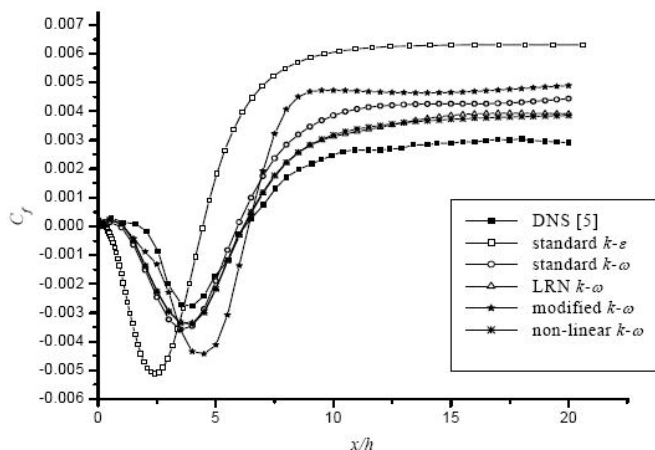
The deformation and vorticity tensors are defined as

$$S_{ij} \equiv \frac{\partial U_i}{\partial x_j} + \frac{\partial U_j}{\partial x_i} \quad \text{and} \quad \Omega_{ij} \equiv \frac{\partial U_i}{\partial x_j} - \frac{\partial U_j}{\partial x_i}$$

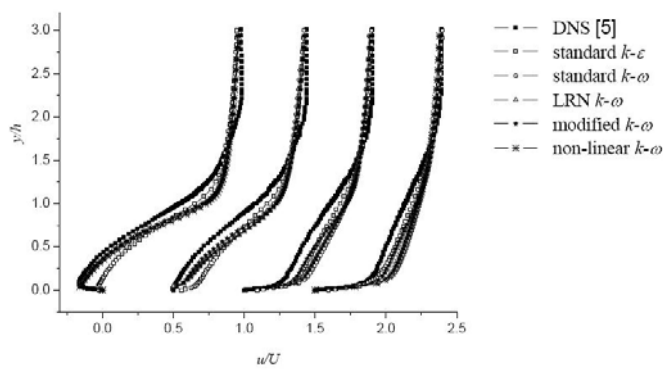
Constants appearing in turbulence model are

$$C_1 = -1, C_2 = 1, C_3 = 2.5,$$

$$\alpha = 0.5, \beta = 0.075, \alpha_0^* = 0.025, \alpha_0 = 0.1, R_\beta = 8, R_k = 6, R_\omega = 2.7$$



(a) Comparison of skin friction coefficient along the bottom wall of the BFS



(b) Comparison of normalised mean velocity profiles at  $x/h = 4, 6, 10$  and  $15$

Figure 2. Validation of turbulence models against BFS.

## 2.2 Numerical details and validation

### 2.2.1 Numerical details

A commercial CFD package FLUENT 6.2.16 is used as a solver to discretise and solve the governing equations. Associated preprocessor GAMBIT 2.2.30 is used for the construction of the computational grid. The QUICK (quadratic upwind interpolation for convective kinematics) scheme is used for the momentum equations and second order upwind differencing scheme for turbulent quantities. SIMPLE (semi implicit method for pressure linked equation) algorithm is used for coupling pressure and velocity terms. Second order implicit scheme is used for time advancement. While standard models and low Re models are available in FLUENT, non-linear  $k-\omega$  and modified  $k-\omega$  models are incorporated in FLUENT through user defined functions (UDFs). The non-linear terms are added as a source term in the momentum and in the equations for turbulent quantities. For the modified  $k-\omega$  model, a cross diffusion term is added as a source term in the  $\omega$  equation. The turbulent viscosity is also made to vary according to the respective governing equations through UDFs. Computations are carried out until solution is converged.

### 2.2.2 Validation

The non-linear  $k-\omega$  model, modified  $k-\omega$  model along with standard models like standard  $k-\omega$  and standard  $k-\epsilon$ , low-Reynolds number (LRN)  $k-\omega$  model are validated against flow through the backward facing step (BFS) at  $Re = 5,100$ , based on the step height,  $h$ . The case studied here is the one that has been studied using DNS by Le *et al.*<sup>(5)</sup>. Fig. 2(a) shows the comparison of normalised skin friction coefficient along the bottom wall. The DNS data shows high levels of skin friction in the reversed flow region which means an energetic mixing producing extremely steep velocity gradient near the wall. In the recirculation region, predictions by the modified  $k-\omega$  and non-linear  $k-\omega$  models show better improvement than those by standard  $k-\omega$  and standard  $k-\epsilon$  models. In the redeveloping region, modified  $k-\omega$  and non-linear  $k-\omega$  slightly deviates from DNS, but comparatively prediction by these models are better than those by standard  $k-\omega$  and standard  $k-\epsilon$  models.

The normalised streamwise velocity profiles,  $u/U$  at four stations viz  $x/h = 4, 6, 10$  and  $15$  are shown in Fig. 2(b). In the recirculation

zone,  $0 \leq x/h \leq 6$ , the  $k-\omega$  family of models predict better than those by  $k-\epsilon$  models. In the redeveloping region, the non-linear  $k-\epsilon$  model gives markedly improved predictions when compared with the other models. Above  $y/h = 1$  the results of all the models match with each other and slightly deviates from the DNS.  $k-\omega$  family models match with the DNS data nearer to the wall i.e. mixing shear layer region ( $y/h < 1$ ). Far from the wall ( $y/h > 1.5$ ) standard  $k-\epsilon$  and non-linear  $k-\epsilon$  models almost matches with DNS data. This implies that the  $k-\omega$  models do well for near wall region and for separated region and standard  $k-\epsilon$  and non-linear  $k-\epsilon$  models do well for high Reynolds number flows or far from near wall regions.

One of the commonly used parameters to justify the accuracy of a turbulence model in BFS case is the reattachment length. For comparison, the reattachment length given by each model is presented in the Table 1. From Table 1 it is observed that prediction by modified  $k-\omega$  and non-linear  $k-\omega$  models are closer to the DNS. Hence the validation of turbulence models chosen for the study is performed and the present problem is carried out.

## 2.3 Boundary conditions

The present problem is studied as 2d axisymmetric case. A flat velocity profile is applied at the inlet. The velocity of air ( $U$ ) used at the inlet condition is  $30\text{ms}^{-1}$ . Along with the velocity, turbulent intensity ( $I$ ) of 3.47% and length scale,  $D_0$  are used as boundary condition at the inlet. In the fluent, the turbulent from these two parameters the values of  $k$  and  $\omega$  are estimated as follows,

$$k = \frac{3}{2}(UI)^2 \quad \text{where } U \text{ is the mean flow velocity}$$

$$\omega = \frac{k^{1/2}}{C_\mu D_0}, \quad \text{where } C_\mu \text{ is a constant.}$$

Neumann condition is used at the outlet and axis boundary condition along the centre line is applied. The usual no slip boundary condition is applied on the wall along the forebody-spindle-afterbody combination.

## 2.4 Grid independence study

In order to get the solution free from influence of the grid, grid independence study was done with nine different grid sizes. Mapped mesh with quadrilateral elements with varying cell sizes in both the

**Table 1**  
Summary of reattachment length for BFS

Models	Reattachment length ( $x_r/h$ )	Deviation (%)
DNS <sup>(3)</sup>	6.28	—
Standard $k-\epsilon$	5.60	11.0
Non-linear $k-\epsilon$	5.80	7.0
LRN $k-\epsilon$	3.58	40.0
Standard $k-\omega$	6.00	4.8
LRN $k-\omega$	6.00	4.8
modified $k-\omega$	6.20	1.3

**Table 2**  
Summary of grid independence test

Grid	cells	Average $C_d$
150×90	11,916	0.17645
300×45	12,340	0.196093
300×90	24,720	0.194601
300×135	36,400	0.189652
300×180	48,900	0.190947
450×90	35,820	0.1975
600×90	47,760	0.198656
450×135	53,700	0.197318
600×180	95,520	0.198212

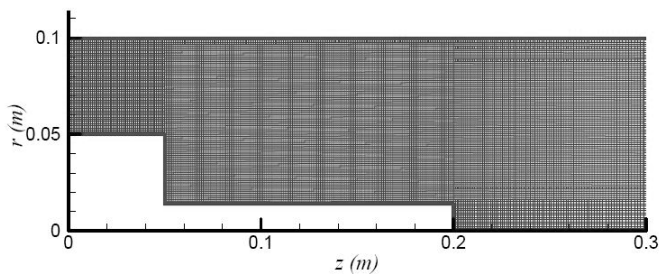


Figure 3. A typical computational grid for standard model.

axial direction ( $z$ ) and radial direction ( $r$ ) were created using FLUENT associated pre-processor software, GAMBIT. For the standard two equation models, wall functions were used to capture the gradients of the flow variable near the walls. For this, the first grid normal to the wall is placed at  $y^+ > 11.225$ , because this value has to meet the requirement for the implementation of the wall function. However, for low Reynolds number (LRN) models, the first grid point should be within  $y^+ < 1$ . This can be achieved by keeping the same number of cells as in standard models, but with increasing stretching factor so that the first point is within the required range. The grid details and the results obtained for the corresponding grids are summarised in the Table 2.

From Table 2, one can say that the result obtained from the grid  $450 \times 90$  shows negligible deviation compared with those of fine grids. So the grid  $450 \times 90$  is considered to be optimum grid and it is used for further analysis.

This grid independence test was done for forebody-spindle combination alone without afterbody. However, the same optimum grid was used for the forebody-spindle-afterbody combination also by retaining the same grid intensity. A typical computational grid employed for standard model is shown in Fig. 3.

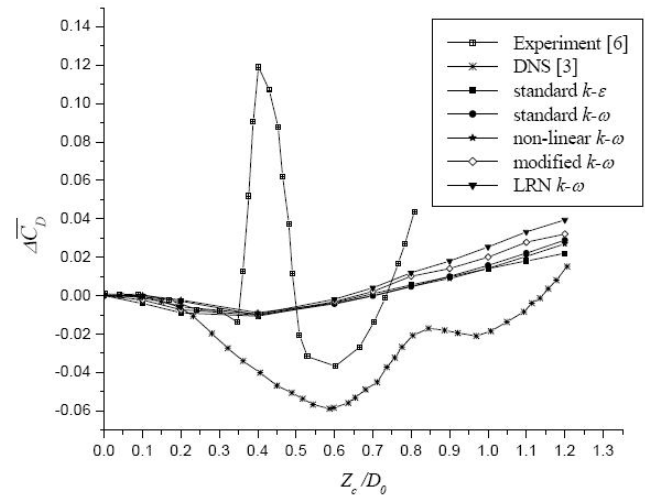


Figure 4. Change in drag coefficient resulting from the addition of afterbody to forebody-spindle combination obtained for DNS for different cavity lengths

## 2.5 Solution convergence

The convergence of the computational solution is determined based on scaled residuals for the continuity, momentum and transport equations. The total residual for a given variable is based on the imbalance in an equation for conservation of that variable summed over all computational cells. The scaled residuals for solution convergence are set to  $10^{-5}$  for all governing equations. The solution is considered to be converged when all of the scaled residuals are less than or equal to this prescribed value.

## 3.0 RESULTS AND DISCUSSION

### 3.1 Drag on forebody-spindle-afterbody combination

The main purpose to study the aerodynamic characteristics of TVC is to get an optimum cavity size formed between the forebody and the afterbody. The minimum drag condition corresponds to steady flowfield inside the cavity as well as behind the afterbody without vortex shedding. So the cavity size corresponding to the minimum drag condition is referred as the optimum cavity size.

The time averaged drag coefficient ( $C_D$ ) on the forebody-spindle-afterbody combination for each case is computed from the given formula

$$\text{Average } C_D, \quad \overline{C_D} = \frac{1}{t_c} \int_0^{t_c} (C_p + C_f) dt \quad \dots (11)$$

where,  $C_p$  and  $C_f$  are the pressure coefficient and skin-friction coefficient respectively. Time  $t_c$  corresponds to the calculated time.

To observe the change in drag due to the addition of afterbody, calculations are first made for the forebody-spindle combination alone. Then calculations were performed on an afterbody-spindle-afterbody combination for different cavity sizes.

Time averaged quantities from these calculations were obtained by averaging the data over a period of 0.46s (twenty flow through time). Calculations were made by five different two equation models. Figure 4 shows the variation in change in drag coefficient ( $\Delta C_D$ ), which is obtained by subtracting the base drag coefficient (without afterbody) from that obtained with the afterbody for different cavity lengths. The drag coefficient decreases initially with

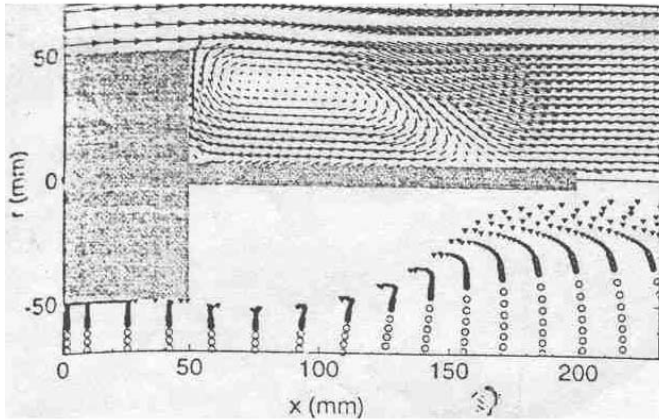


Figure 5. Instantaneous flowfield obtained using DNS for the forebody-spindle combination alone. (Katta and Roquemore<sup>(3)</sup>).

the separation between the forebody and afterbody and then increases for large separations. The experimental and DNS results show that the drag reduction is maximum when the disk is placed at  $0.6D_0$  downstream of the forebody. On the other hand, results obtained from all the two equation models show that the drag reduction is maximum when the afterbody is placed at  $0.4D_0$  downstream of the forebody. The calculated drag coefficient decreases to a minimum value and then increases gradually for cavity lengths greater than  $0.4D_0$ . A large spike in the drag coefficient profile was observed in the experiment. Present calculations by turbulence models and as well as DNS<sup>(3)</sup> do not capture this spike.

While the turbulence models solve the averaged quantities, DNS simulates instantaneous quantities. The inlet condition also plays a major role in the results. In this work, a uniform velocity with

**Table 3**  
Reattachment lengths obtained by different turbulence models

Models	Reattachment length from the forebody $z_r$ (mm)
DNS <sup>(3)</sup>	110
Standard $k-\epsilon$	100
Standard $k-\omega$	100
Modified $k-\omega$	95
Non-linear $k-\omega$	112

turbulent intensity and length scale is used, whereas in DNS, a driver channel is used to obtain instantaneous inlet condition. Further, other numerical strategies like grid size and discretisation scheme are different in both approaches. These are possible reasons for the deviation in the results obtained by DNS and the turbulence models.

### 3.2 Flow structures

#### 3.2.1 Forebody-spindle alone

The velocity vector plots and streamline plots are the effective tools to visualize the flowfields. The instantaneous solution obtained using DNS (Katta and Roquemore<sup>(3)</sup>) for the forebody-spindle combination (without afterbody) is shown in Fig. 5. Velocity vector is shown in the upper half and a particle distribution is shown on the lower half. It is observed from these figures that the flowfield is nearly steady state, with a large recirculation zone extends up to  $z = 160\text{mm}$  created downstream of the forebody.

The streamline plots for the forebody-spindle geometry obtained using different two equation turbulence models are given in Fig. 6. This instantaneous solution using turbulence models are obtained at

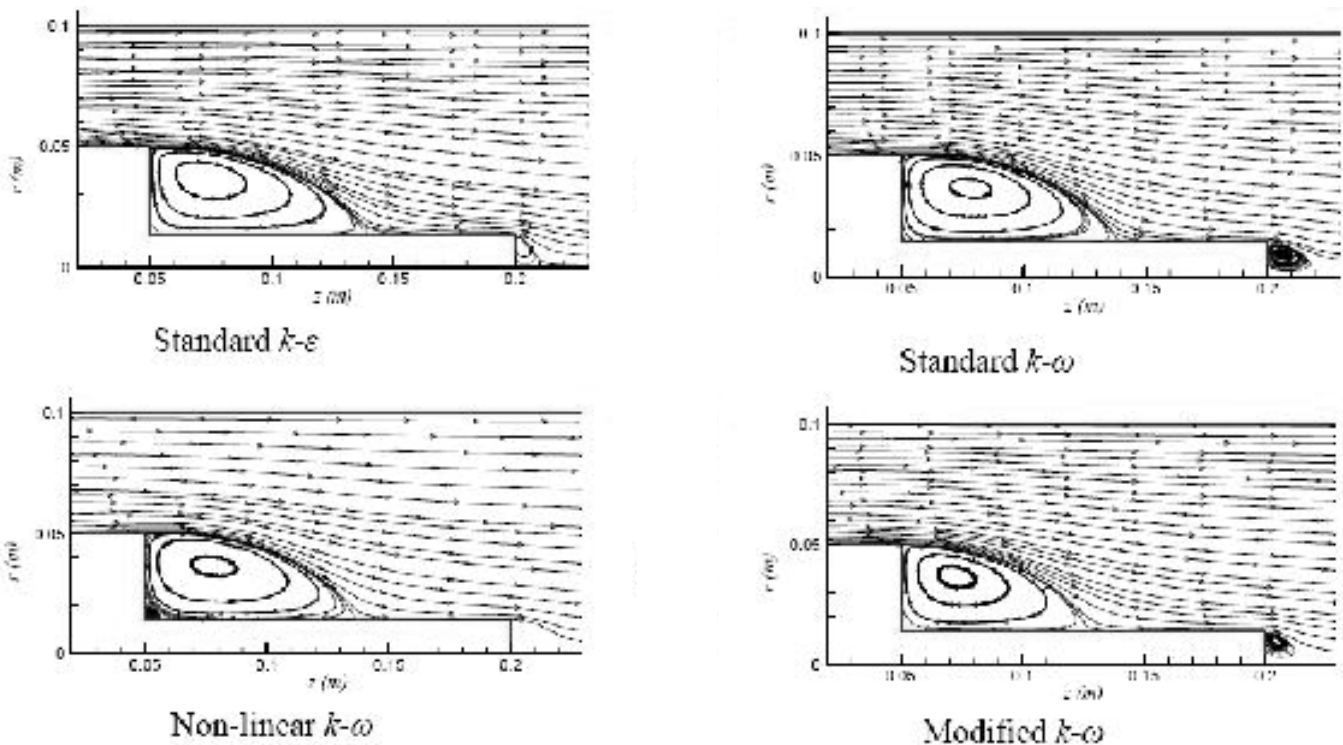


Figure 6. streamline plots for forebody-spindle combination alone.

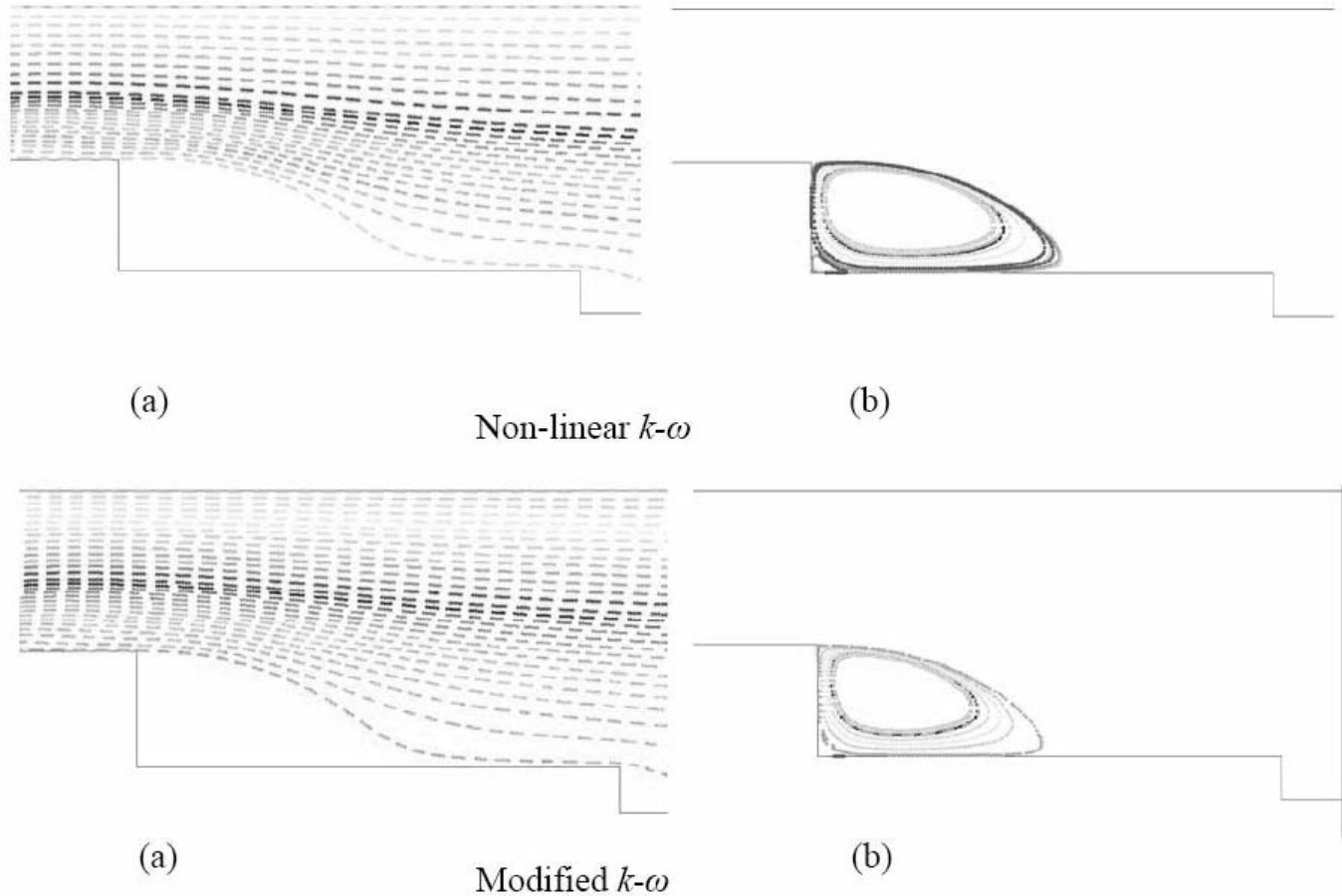


Figure 7. Particle distributions for forebody-spindle combination alone  
 (a) Particles released from the entrance (b) Particles released in the recirculation region.

the end of thirty flow through time. A small vortex is developed in the corner of the forebody and the spindle in the DNS case. From Fig. 6, it is observed that non-linear  $k-\omega$  model alone captures this corner vortex, while all the other models failed to capture. Table 3 presents the reattachment length obtained by all the models. From Table 3, it is observed that the reattachment length obtained by non-linear  $k-\omega$  closely matches with that obtained by DNS.

In order to study the dynamic nature of the flow, the instantaneous positions of the particles that were continuously released from locations near the entrance region and inside the recirculation region obtained by non-linear  $k-\omega$  and modified  $k-\omega$  model are shown in Fig. 7. From these particle distribution plots, it is evident that the flowfield is steady. It is observed that none of the particles injected into freestream entered the recirculation region formed behind the forebody. On the other hand, the particles that were injected into the recirculation region remained within the recirculation zone itself.

### 3.2.2 Forebody-spindle-afterbody

Without the addition of afterbody, the geometry is similar to the flow through backward facing step and gives steady nature of the flowfield. Perturbation to this steady flow can be obtained by placing an afterbody on the spindle. Figure 8 shows the instantaneous flowfields obtained using DNS. In that, upper half shows the velocity vector plot and the lower half shows the particle distribution. Figure 9 shows the comparison of streamlines obtained using modified  $k-\omega$  and non-linear  $k-\omega$  models for different cavity sizes.

The instantaneous solution obtained using the turbulence models at the end of thirty flow through time. In general, vortices are formed in the cavity and downstream of the afterbody in all the cases. The instantaneous time by DNS and turbulence models are not the same which could be reason in slight variation in the flowfield when compared.

When the cavity formed between the forebody and the afterbody is small as in the case of  $Z_d/D_0 = 0.2$ , many vortices are formed inside the cavity as observed from Fig. 9(a). The largest vortex in the cavity is rotating in the direction opposite (counter clockwise direction) that of the recirculating vortex for forebody-spindle alone case. From the particle traces plot given in Fig. 10(a), it is observed that some of the particles that are released inside the recirculation region comes out along with shedding from the disk and combines with the particles that are released in the freestream. This shows that the flowfield inside and behind the cavity is not in steady state. The unsteady nature of these cavity vortices triggers shedding of the large recirculating vortex formed behind the afterbody which probably results in maximum drag condition. But this type of flowfield is reported for  $Z_d/D_0 = 0.4$  by Katta and Roquemore<sup>(3)</sup> using DNS (Fig. 8(a)). However, by turbulence models for  $Z_d/D_0 = 0.4$ , (Fig. 9(b)) a single vortex in the cavity and another behind the disk is obtained. The direction of rotation of the cavity vortex is clockwise as observed in the case of forebody-spindle alone.

The experimental data and DNS calculations show that the minimum drag condition was obtained when the disk was located at  $Z_d/D_0 = 0.6$ . The flow inside the cavity became steady as a result, the flow behind the disk also became nearly steady. Even though two

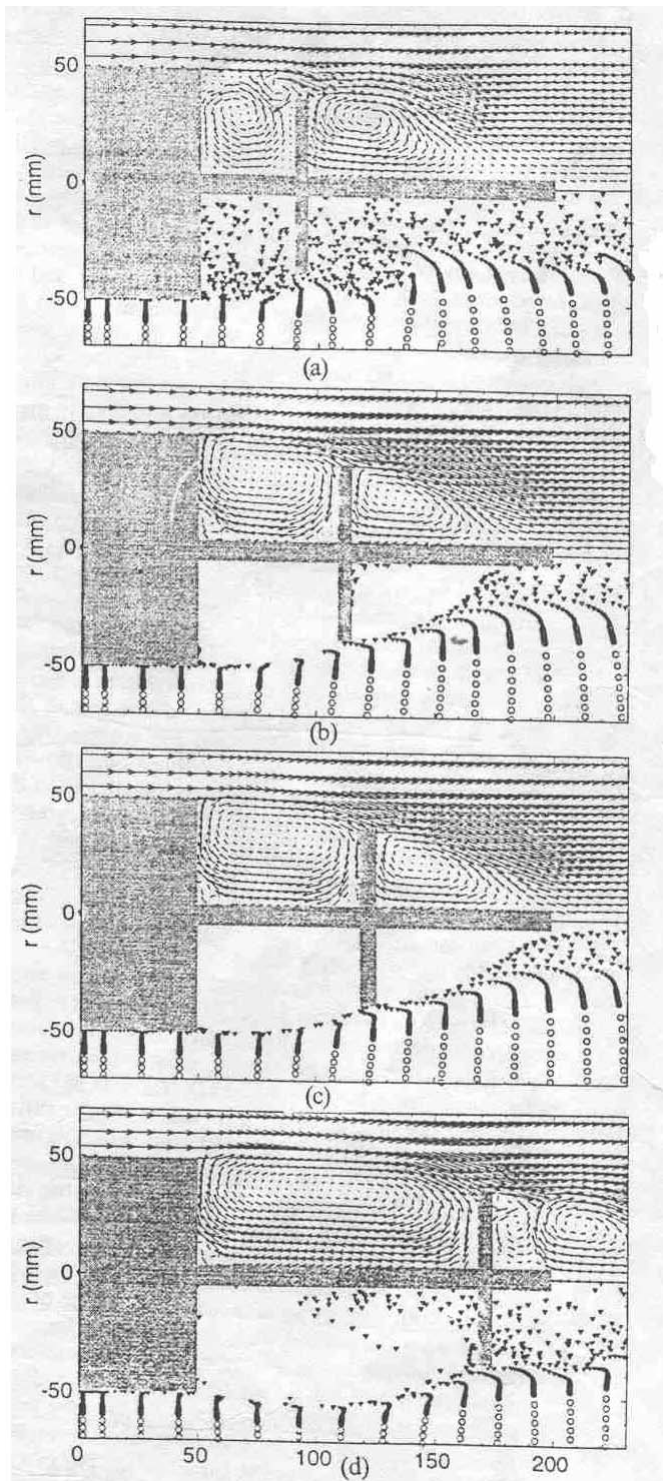


Figure 8. Instantaneous flowfield obtained using DNS for different cavity lengths  $Z_c/D_0 =$  (a) 0.4, (b) 0.6, (c) 0.7 and (d) 1.2. Velocity vectors and particle distributions are shown in upper and lower halves respectively. (Katta and Roquemore<sup>(3)</sup>).

equation models capture the steady flowfield inside the cavity when the disk is located at  $Z_c/D_0 = 0.6$ , the minimum drag condition was obtained when the disk is placed at  $Z_c/D_0 = 0.4$ .

Existence of well defined corner vortices both near the forebody and the afterbody was reported in the DNS. The non-linear  $k-\omega$  model captures the corner vortices near the forebody alone as

observed in the Fig. 9. But all the other models fail to capture the corner vortices.

The steady vortices in the cavity and behind the disk in the case of  $Z_c/D_0 = 0.6$  act like a dividing streamline. The flowfield near the tip of the disk shows that the fluid is passing around the afterbody smoothly. However, the location of the main-flow re-attachment point on the spindle has shifted from 112mm to 120mm from the forebody with the addition of the disk for non-linear  $k-\omega$  case. For DNS it is shifted from 110mm to 125mm. This increase in the reattachment distance was also observed in the flow-visualisation experiments by Little and Whipkey<sup>(6)</sup>.

Results obtained by two equation models for  $Z_c/D_0 = 0.7$  yielded perfectly steady vortices within the cavity and also behind the afterbody which are same as observed by DNS. For cavity sizes greater than  $Z_c/D_0 > 0.7$ , the drag coefficient increases drastically due to unsteady flowfield inside and behind the cavity. Unlike in the smaller than optimum cavity size, only one dominating vortex was formed in the cavity. The vortex in this larger-than-optimum cavity case is not shedding. However, since the cavity size is larger, the trapped vortex recirculates within the cavity. This is observed from the particle distribution as well as streamline plot. Interestingly, the streamline drawn from the edge of the forebody given in Figs 9(e) and 10(e) shows that the flow dips slightly into the cavity near the disk and then flows back around the tip of the disk as reported using DNS. This dividing streamline also suggests that no flow is entering the recirculation region.

### 3.3 Residence time and entrainment characteristics

A stable vortex can be obtained inside the cavity by placing the afterbody at an appropriate place. It is also observed that, the main flow does not entrain into the cavity. In an actual combustor, this means that the transport of oxidizer from the main flow into the cavity is very low. To initiate combustion, fuel is injected inside the cavity. Because of the poor oxidizer entrainment from the main flow into the cavity, results in poor air-fuel mixture which would reduce the performance of the combustor. In order to accommodate the decrease in the oxidizer, additional air known as 'primary air' must be fed into the cavity directly to obtain better performance from the trapped vortex combustor. Therefore, it is important to understand the residence time and the entrainment characteristics for different cavity sizes.

#### 3.3.1 Residence time characteristics

The residence time is calculated by injecting massless particles at different locations inside the cavity formed between the forebody and the afterbody. The particles are injected into the upper and lower halves of the vortex that are formed inside the cavity. The different locations where the particles are injected for different cavity lengths non-dimensionalised with forebody diameter ( $D_0$ ) are given in Table 4.

Residence time is inversely proportional to the decay time. The time taken by the particles to remain inside the cavity as a function of time taken to reach the complete domain (outlet) by that particle for different cavity size is given in the Table 5. The position of particles released from different locations inside the cavity for different cavity sizes computed by non-linear  $k-\omega$  is given in the Fig. 11. The observations made from the residence time characteristics are as follows:

When the particle is injected at the injection-1 location, the particle takes a less time to remain in the cavity. The residence time for the cavity size  $Z_c/D_0 = 0.6$  is comparatively higher than that of  $Z_c/D_0 = 0.4$ .

Interestingly, when the particles are injected nearer to the disk location, none of the particles remain inside the cavity for the cavity length of  $Z_c/D_0 = 1.2$  as shown in Fig. 11. The residence time for  $Z_c/D_0 = 0.4$  and  $Z_c/D_0 = 0.6$  shows not much variation for this case. When the particle is injected at the lower half of the vortex

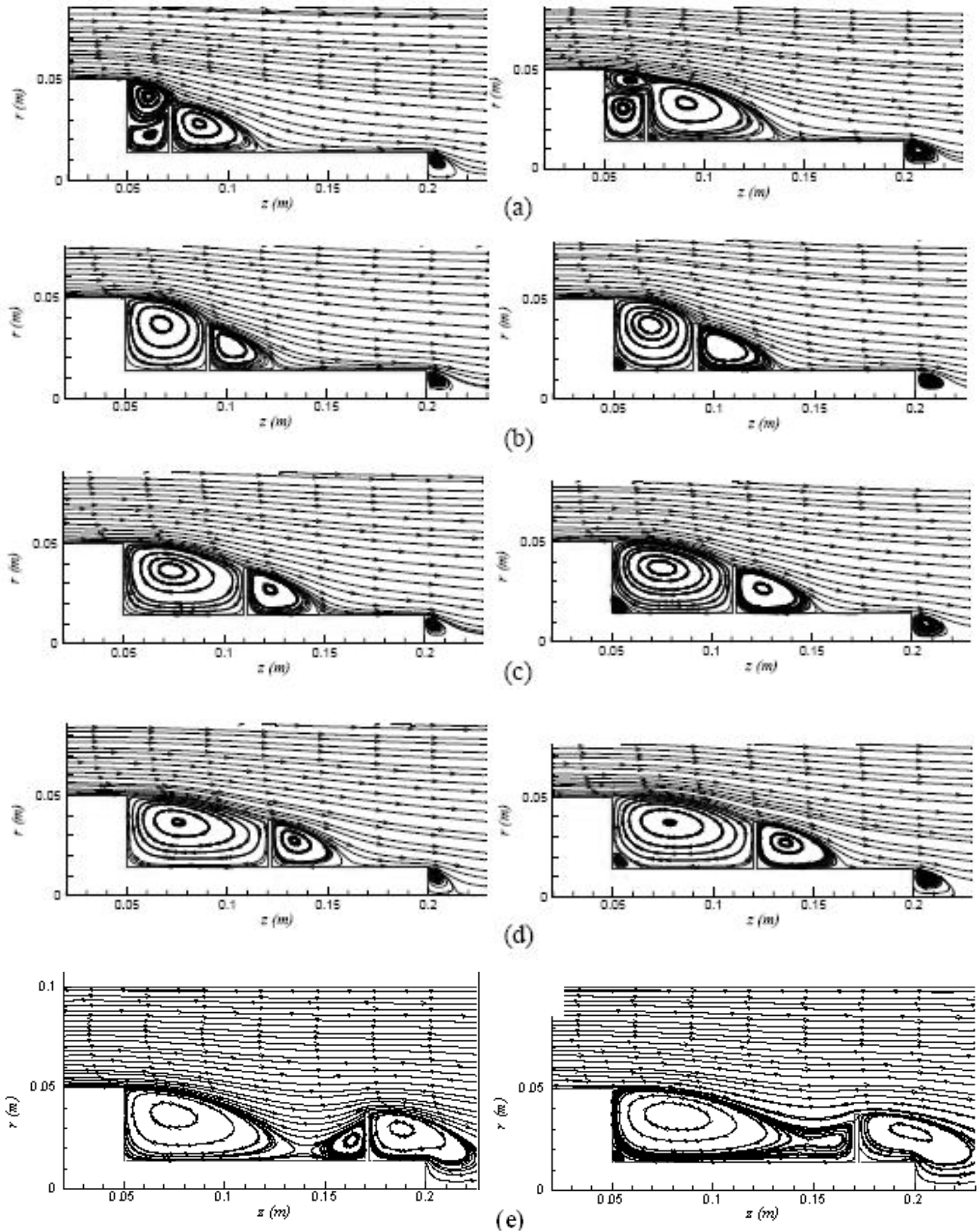


Figure 9. Comparison of streamlines obtained using modified  $k-\omega$  and non-linear  $k-\omega$  for forebody-spindle-disk combination for various disk locations.  $Z_c/D_0 =$  (a) 0.2, (b) 0.4, (c) 0.6, (d) 0.7 and (e) 1.2.

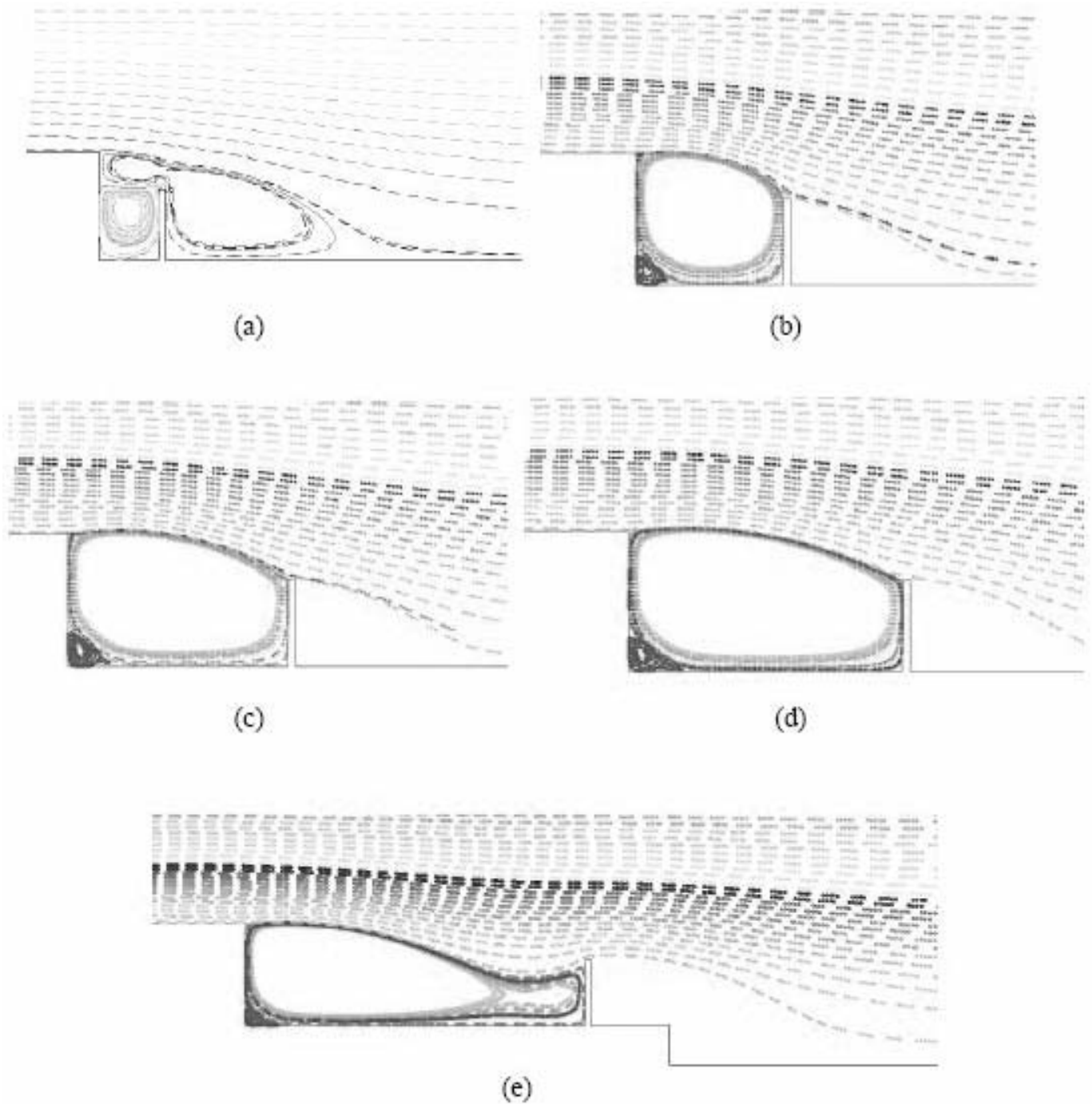


Figure 10. Particle distributions obtained using non-linear  $k-\omega$  model for various cavity lengths formed between forebody and disk.  $Z/D_0 =$  (a) 0.2, (b) 0.4, (c) 0.6, (d) 0.7 and (e) 1.2.

(injection-5) the particles remain inside the cavity for all the time. The particles injected at the upper half of the vortex (injection-4) remain comparatively less time inside the cavity for different cavity lengths. Therefore, the particles injected to the vortices in the upper half have less residence time, while the particles injected in the lower vortices remain for a longer period of time. Same information

was reported in DNS<sup>(9)</sup>. Because of the differences in the residence time of the particle injected from different locations within the cavity, uniform combustion within the cavity is possible by injecting fuel and air into the cavity at multiple locations with varying flow rates.

**Table 4**  
Co-ordinate information for different injection points inside the cavity

	$z$ co-ordinate(m)	$r$ co-ordinate(m)
Injection-1	$0.52D_0$	$0.45D_0$
Injection-2	$0.05D_0$ before the disk	$0.37D_0$
Injection-3	$0.52D_0$	$0.15D_0$
Injection-4	Centre of cavity ( $X_c/2$ )	$0.2D_0$
Injection-5	Centre of cavity ( $X_c/2$ )	$0.36D_0$

**Table 5**  
Residence time of injected particles inside the cavity

	Time taken to remain inside the cavity as a percentage of time taken to reach the outlet		
	$Z_c/D_0 = 0.4$	$Z_c/D_0 = 0.6$	$Z_c/D_0 = 1.2$
Injection-1	49	60	83.4
Injection-2	71.2	67.6	0
Injection-3	100	100	100
Injection-4	68	76	88
Injection-5	100	100	100

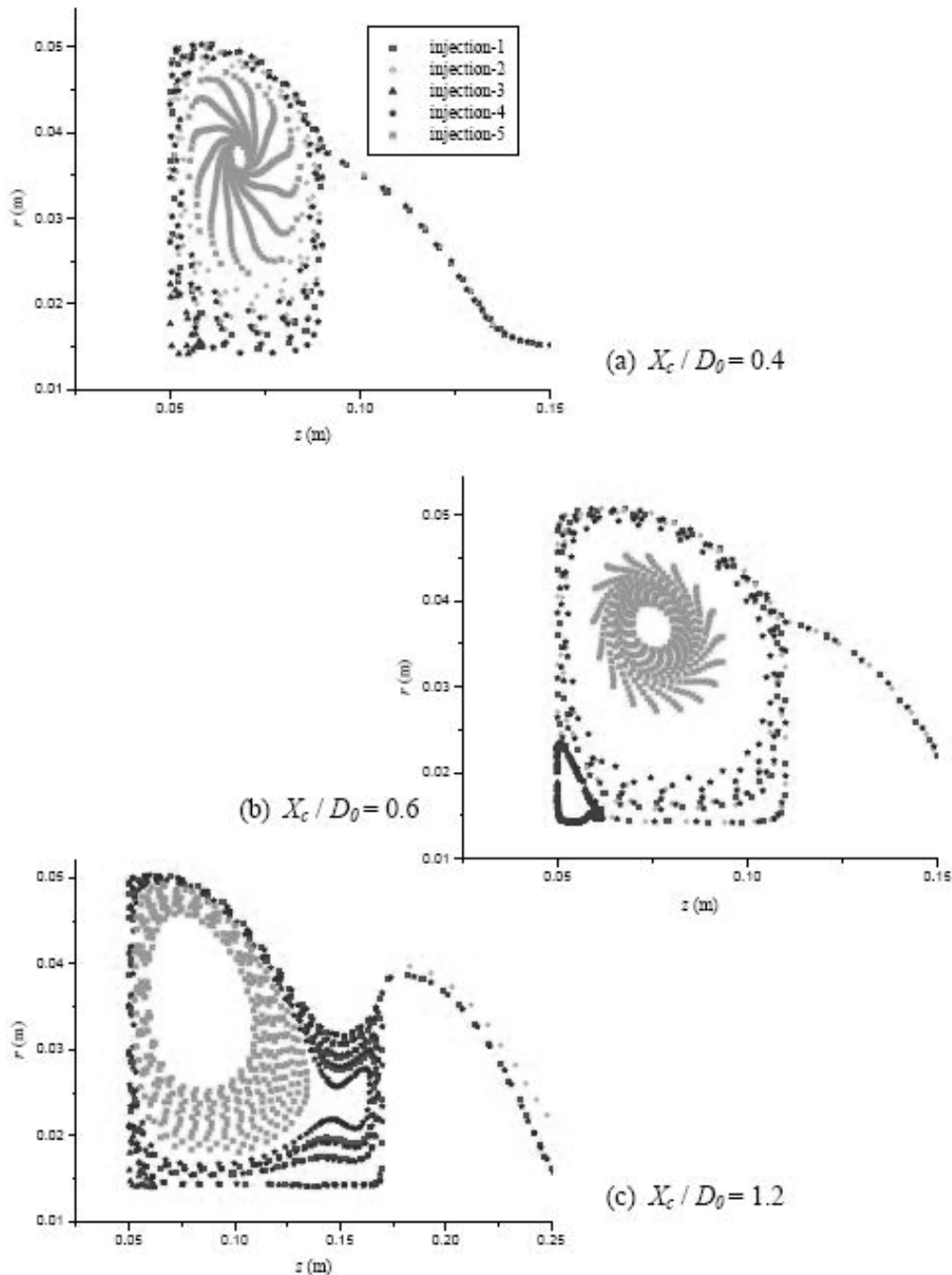


Figure 11. Positions of particles released at different locations inside the cavity obtained using non-linear  $k-\omega$  model for different cavity sizes. Legends are same for all cavity sizes.

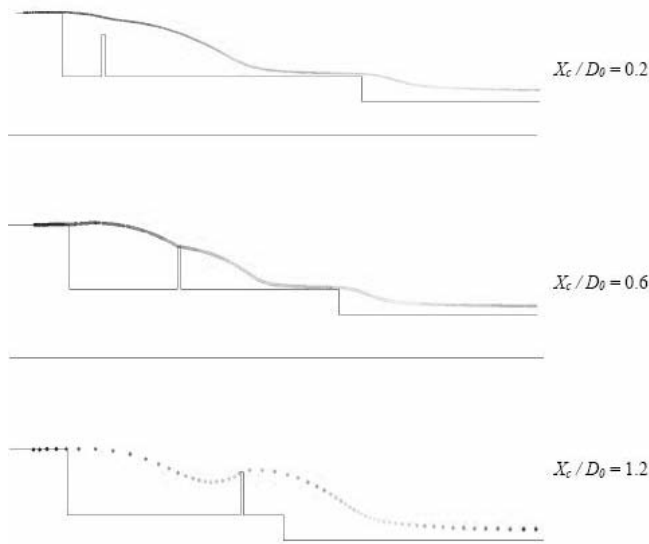


Figure 12. Entrainment characteristics obtained by non-linear  $k-\omega$  model for different cavity lengths.

### 3.3.2 Entrainment characteristics

For bringing the main air/fuel into the cavity, it is important to know the entrainment characteristics of the vortices for different cavity sizes. In order to study the entrainment characteristics of the cavity, a group of massless particles are released from the freestream very close to the top of the forebody. This particle tracking obtained using non-linear  $k-\omega$  for different cavity sizes are shown in Fig. 12.

Katta and Roquemore<sup>(3)</sup> reported that for other than optimum cavity size, some of the particles that are released from the freestream enter the cavity. For optimum cavity size, very little main flow is entrained into the cavity. In the present calculations, for all cavity sizes no entrainment of main flow into the cavity is observed. This emphasizes the main aspect of trapped vortex combustor – that is under optimum design condition, fuel and air necessary for efficient combustion should be directly injected into the cavity without relying on the entrainment from main flow.

## 4.0 CONCLUSIONS

Numerical simulations to study the cold flow through trapped vortex combustor using turbulence models have been carried out. Special focus

is made on the applicability of modified  $k-\omega$  and non-linear  $k-\omega$  turbulence models. The highlights of the present simulations are given below.

- All turbulence models showed maximum drag reduction when the cavity size is 0.4 times the forebody diameter ( $D_0$ ). The optimum cavity size obtained by DNS is  $0.6D_0$ .
- The non-linear  $k-\omega$  obtained a steady state with a large recirculation zone extends up to a reattachment length of 112mm from the forebody on the spindle. The reattachment length obtained by DNS is 110mm from the forebody.
- Non-linear  $k-\omega$  model alone captures the corner vortices inside the cavity that are observed in the DNS calculation.
- The massless particles that are injected in the main flow do not entrain into the cavity. This entrainment characteristics emphasize the need for primary air injection directly into the cavity to improve the performance of the TVC.
- The performance of non-linear  $k-\omega$  is better than other turbulence models for passive flow in the TVC.

The non-linear  $k-\omega$  model employed in this study is quadratic model. Better performance can be obtained when this is made as cubic model and or by tuning the model constants employed. With these satisfied results for the cold flow, this model can be applied for the reacting flow analysis of trapped vortex combustor.

## REFERENCES

1. BREDBERG, J., PENG, S.H. and DAVIDSON, L. An improved  $k-\omega$  turbulence model applied to recirculating flows, *Int J Heat and Fluid Flow*, 2002, **23**, pp 731- 743.
2. HSU, K.Y., GOSS, L.P. and ROQUEMORE, W.M. Characteristics of a trapped vortex combustor, *J Propulsion and Power*, 1998, **14**, (1), pp 57-65.
3. KATTA, V.R. and ROQUEMORE, W.M. Numerical studies on trapped vortex concepts for stable combustion, *J Eng for Gas Turbines and Power*, 1998, **120**, pp 61-68, Trans ASME.
4. KATTA, V.R. and ROQUEMORE, W.M. Study on trapped vortex combustor – Effect of injection on flow dynamics, *J Propulsion and Power*, 1998, **14**, (3), pp 273-281.
5. LE, H., MOIN, P. and KIM, J. Direct numerical simulation of turbulent flow over a backward facing step. *J Fluid Mechanics*, 1997, **330**, pp 349-375.
6. LITTLE, B.H. and WHIPKEY, R.R. Locked-vortex afterbodies, *J Aircr*, 1979, **16**, pp 296-302.
7. POPE, S. *Turbulent Flows*, 2000, Cambridge University Press.
8. SONG, B. and AMANO, R.S. Application of non-linear  $k-\omega$  model to a turbulent flow inside a sharp U-bend, *Computational Mechanics*, 2000, **26**, pp 344-351.
9. STONE, C. and MENON, S. Simulation of fuel-air mixing and combustion in a trapped vortex combustor, 2000, AIAA paper 2000-0478.
10. WILCOX, D.C. *Turbulence Modeling for CFD*, 2006, Third edition, DCW Industries.